Space group symmetries of the phases of $(Pb_{0.94}Sr_{0.06})(Zr_xTi_{1-x})O_3$ across the antiferrodistortive phase transition in the composition range $0.620 \lesssim x \lesssim 0.940$

Ravindra Singh Solanki,[1] Anatoliy Senyshyn,[2] and Dhananjai Pandey[1,*]

[1]*School of Materials Science and Technology, Indian Institute of Technology (Banaras Hindu University), Varanasi-221005, India*

[2]*Forschungsneutronenquelle Heinz Maier-Leibnitz (FRM II), Technische Universität München, Lichtenbergstrasse 1, D-85747 Garching bei München, Germany*

(Received 27 June 2014; revised manuscript received 15 September 2014; published 29 December 2014)

The existing controversies about the space group symmetries of $Pb(Zr_xTi_{1-x})O_3$ (PZT) above and below the antiferrodistortive (AFD) phase-transition temperature (T_{AFD}) in the Zr^{4+}-rich ($0.620 \lesssim x \lesssim 0.940$) compositions are addressed using the results of dielectric, synchrotron x-ray powder diffraction (SXRPD) and neutron powder diffraction (NPD) studies. These compositions undergo an AFD phase transition above room temperature due to tilting of oxygen octahedra leading to a superlattice phase of PZT. We have substituted 6% Sr^{2+} at a Pb^{2+} site to enhance the tilt angle and thereby the intensity of the superlattice peaks. The real and imaginary parts of the complex dielectric permittivity have been used to locate the paraelectric to ferroelectric and ferroelectric to AFD phase transitions. Rietveld analysis of SXRPD and NPD profiles unambiguously reject the rhombohedral phases in the $R3c$ and $R3m$ space groups below and above T_{AFD}, respectively, with or without a coexisting monoclinic phase in the Cm space group and confirm that the true symmetries are monoclinic in the Cc and Cm space groups below and above T_{AFD}, respectively. Based on these and previous findings a phase diagram of PSZT for $0.40 \leqslant x \leqslant 0.90$ showing stability fields of monoclinic Cc and monoclinic Cm, tetragonal $P4mm$, and cubic $Pm\bar{3}m$ phases has also been presented.

DOI: 10.1103/PhysRevB.90.214110 PACS number(s): 77.84.Cg, 61.05.cp, 61.05.fm

I. INTRODUCTION

Structural phase transitions in perovskites are broadly classified as ferrodistortive (FD) and antiferrodistortive (AFD) types depending on whether they are driven by the freezing of a zone center ($\vec{k} = 0$) or a zone boundary ($\vec{k} \neq 0$) phonon mode [1,2]. The classic examples of FD phase transitions are the ferroelectric phase of $PbTiO_3$, $KNbO_3$, $BaTiO_3$ resulting from the freezing of the Γ_4^- ($k = 0,0,0$) mode of the paraelectric cubic $Pm\bar{3}m$ phase [3]. Whereas the AFD transitions are ubiquitous in perovskite, the most investigated example is the tilt transition involving antiphase rotation of oxygen octahedra in the tetragonal phase of $SrTiO_3$ below $T_c \sim 105$ K resulting from the freezing of the R_4^+ ($k = 1/2,1/2,1/2$) mode of the cubic $Pm\bar{3}m$ phase [4,5]. AFD phase transitions can also result in in-phase rotation of oxygen octahedra driven by the M_3^+ ($k = 1/2,1/2,0$) mode of the cubic phase as has been reported in $KMnF_3$ [6]. There are several examples of perovskites where both FD and AFD phase transitions occur one after the other at two different characteristic temperatures, such as in $(Sr_{0.96}Ca_{0.04})TiO_3$ where a ferrielectric phase results from successive freezing of one of the components of the R_4^+ mode and Γ_4^- mode of the cubic paraelectric phase on lowering the temperature below 225 and 34 K, respectively [7]. In the solid solutions of the well-known multiferroic $BiFeO_3$, experimental observations suggest that both the R_4^+ and the Γ_4^- modes freeze at the same temperature causing a cubic $Pm\bar{3}m$ to rhombohedral $R3c$ phase transition [8].

The paraelectric cubic phase of the technologically important solid solutions of $PbTiO_3$ with $PbZrO_3$, i.e., $Pb(Zr_xTi_{1-x})O_3$ (commonly known as PZT), also undergoes FD (ferroelectric) and AFD structural phase transitions. In addition, PZT shows a composition-induced morphotropic phase transition from the tetragonal phase with the $P4mm$ space group stable for $0.00 \leqslant x < 0.515$ to a pseudorhombohedral monoclinic phase with the Cm space group stable for $0.530 < x \leqslant 0.620$ through a composition range of $0.520 \lesssim x \lesssim 0.530$ over which a pseudotetragonal monoclinic phase in the Cm space group is stable at room temperature [9,10].

There are two different classes of technologically useful PZT ceramics. The PZT compositions lying very close to the morphotropic phase boundary (MPB), across which there is a composition-induced tetragonal to monoclinic phase transition, show pronounced piezoelectric activity and are therefore widely used for electromechanical sensing and actuating devices [11]. The PZT compositions away from the MPB on the Zr^{4+}-rich side of the MPB, on the other hand, show large pyroelectric coefficients useful for infrared detector applications [11]. The ground state of PZT for the entire range of compositions with tetragonal structures, except those very close to the MPB, is decided by the ferrodistortive transition resulting from the freezing of the polar Γ_4^- mode. However, the technologically important PZT compositions are not the ones with the tetragonal ground state. The ground state of both the strongly piezoelectric and the pyroelectric PZT compositions is decided not by the FD transition but by AFD transition resulting from the freezing of the R_4^+ mode involving antiphase rotation of the oxygen octahedra.

In the technologically important piezoelectric ceramic compositions near the MPB, the Curie transition from the paraelectric cubic to the ferroelectric tetragonal phase resulting from the freezing of one of the components of the Γ_4^- mode is followed by another structural phase transition driven by the freezing of the remaining two components of the Γ_4^- mode. This structural transition occurs due to the slightly tilted nature

*Corresponding author: dp.mst1979@gmail.com

of MPB towards the Zr^{4+}-rich side and was investigated in detail by Mishra *et al.* [12,13] above room temperature and by Noheda *et al.* [14] below the room temperature. Following the pioneering paper by Noheda *et al.* [14], the low-temperature ferroelectric phase resulting from the tetragonal ferroelectric phase is now known to be monoclinic in the *Cm* space group with a pseudotetragonal character. However, as shown by Ragini *et al.* [15] and Ranjan *et al.* [16], this *Cm* phase is not the ground state of PZT in the MPB region since it undergoes an AFD transition to a superlattice phase which obviously constitutes the ground state of PZT for compositions close to the MPB. For the pyroelectric compositions with $0.620 \lesssim x \lesssim 0.940$ the AFD transition occurs below the Curie point (T_c) but above the room temperature as has been known for several decades [11].

Historically, the structure of the ferroelectric phases of PZT above and below the AFD phase transition temperature (T_{AFD}) in the composition range of $0.620 \lesssim x \lesssim 0.940$ has been believed to correspond to the rhombohedral phase in the *R*3*m* and *R*3*c* space groups [11], respectively. However, following the work of Ragini *et al.* [9] and Singh *et al.* [10], it is now widely accepted that the true space group symmetry of the ferroelectric *R*3*m* phase is monoclinic in the *Cm* space group, even though it shows a pseudorhombohedral feature for $0.530 < x < 0.620$ at room temperature. Pandey *et al.* [17] have proposed that the correct space group symmetry of the high-temperature ferroelectric phase in the composition range of $0.620 \lesssim x \lesssim 0.940$ below the Curie point is also *Cm*. It is the monoclinic phase in the *Cm* space group that undergoes an AFD transition to a superlattice phase for compositions close to the MPB in which the *Cm* phase has got a pseudotetragonal feature as also for the Zr^{4+}-rich compositions for which the monoclinic phase has got pseudorhombohedral character.

What is the space group symmetry of the superlattice ground-state phase of PZT? The space group of the superlattice phase for the MPB compositions was shown to be *Cc* by Hatch *et al.* [18], which was confirmed by several other workers both experimentally [19–22] and theoretically [23]. Subsequently, some workers raised doubts about the correctness of the *Cc* space group for the superlattice phase and as an alternatively proposed *R*3*c* space group. Since this rhombohedral phase in the *R*3*c* space group could not explain the splitting of the $(200)_{pc}$ (pc represents pseudocubic) peak, they postulated a coexisting monoclinic phase in the *Cm* space group. The controversy between the *Cc* and the *R*3*c* + *Cm* space group models has been recently resolved unambiguously in favor of the *Cc* space group using 6% Sr^{2+}-substituted [22] and in pure PZT samples [24].

Pandey *et al.* [17] have proposed that the space group of the superlattice phase below the AFD transition in the composition range of $0.620 \lesssim x \lesssim 0.940$ should also be *Cc*. Fraysse *et al.* [25] in a recent neutron powder diffraction study have also proposed the *Cc* space group for this composition range. However, recently several workers [26] have questioned the *Cc* space group below T_{AFD} in this composition range. According to these workers, two ferroelectric phases in the space groups *R*3*m* and *Cm* and *R*3*c* and *Cm* coexist above and below T_{AFD}, respectively. This proposal implies that the AFD transition involves a change in space group from *R*3*m* to *R*3*c*. Although the *R*3*c* to *R*3*m* AFD phase transition has been known and accepted for several decades [11,27,28], the origin and the role of the coexisting monoclinic phase in the *Cm* space group below and above T_{AFD} remains unexplained. Why does only the *R*3*m* phase undergo an AFD transition and not the *Cm* phase, even though both are ferroelectric with untilted oxygen octahedra, is also not clear?

The present work was undertaken to resolve the existing controversies about the structure of the ground-state phase of PZT on the Zr^{4+}-rich side in the composition range of $0.620 \lesssim x \lesssim 0.940$ using synchrotron x-ray powder diffraction (SXRPD), neutron powder diffraction, and dielectric studies. We have analyzed Zr^{4+}-rich compositions of 6% Sr^{2+}-substituted PZT, i.e., $(Pb_{0.94}Sr_{0.06})(Zr_xTi_{1-x})O_3$ (PSZT), with $x = 0.65, 0.70, 0.80, 0.85$, and 0.90. Since Sr^{2+} substitution decreases the average cationic radius of the "*A*" site in the ABO_3 perovskite structure, it is expected to increase the tilt angle [29,30] and concomitantly the intensity of the superlattice peaks [31]. Furthermore, to establish the structure of the high-temperature phase of these compositions, we have chosen a representative composition of PSZT with $x = 0.65$ and analyzed SXRPD patterns as a function of temperature. Our results unambiguously reject the possibility of *R*3*m* to *R*3*c* AFD transition with or without the coexisting monoclinic *Cm* phase. It is shown that the AFD transition occurs between a monoclinic phase in the *Cm* space group stable for $T_{AFD} < T < T_c$ and another monoclinic phase in the *Cc* space group below $T < T_{AFD}$ over the entire composition range of $0.620 \lesssim x \lesssim 0.940$. We also use the present results in conjunction with our previous results [32] to extend the phase diagram proposed earlier by us in the MPB region [32] to the Zr^{4+}-richer side.

II. EXPERIMENT AND ANALYSIS

Samples of PSZT for $0.65 \leqslant x \leqslant 0.90$ were prepared by a solid-state reaction route. Stoichiometric mixtures of analytical reagent grade $PbCO_3$ (99%), $SrCO_3$ (99%), ZrO_2 (99%), and TiO_2 (99%) were calcined at 1073 K for 6 h in an open alumina crucible and were sintered at 1323 K for 6 h in closed alumina crucibles using $PbZrO_3$ as the spacer powder. The weight loss in the samples after sintering was $\lesssim$0.1%.

Temperature-dependent SXRPD measurements in the 300–620 K range and at room temperature were carried out at the P02.1 hard x-ray diffraction beam line of PETRA III, DESY, Germany at a wavelength of 0.207 12 Å (~60 keV). Data were collected at a step of 0.007° in the 2θ range from 1.5° to 11°. Neutron diffraction data at room temperature on the same samples were obtained from FRMII, Garching, Germany using the high-resolution SPODI powder diffractometer [33] at a wavelength of 2.536 Å.

Rietveld analysis of the neutron and synchrotron x-ray powder diffraction patterns was carried out using the FULLPROF [34] software package.

For dielectric measurements, fired-on silver electrodes were applied after gently cleaning the surfaces of the pellets using 0.25-μm diamond paste. The temperature-dependent dielectric measurements were carried out at a heating rate of 1 K/min using a Novocontrol Alpha-*A* high performance frequency analyzer and a Eurotherm 2404 programmable temperature controller. The sample temperature during the dielectric

measurements was varied using a homemade high-temperature furnace and was controlled within ±1 K using an Eurotherm-2404 programmable temperature controller.

III. RESULTS AND DISCUSSION

In our previous paper [22], samples were prepared by a semiwet route, and it has been shown that the MPB in PSZT lies in the composition range of $0.520 \lesssim x \lesssim 0.535$ (Fig. 1 of Ref. [22]) whereas it lies in the range of $0.515 < x < 0.530$ for pure PZT prepared by the same method [9,17]. The physical properties show a peak at $x = 0.530$ for PSZT with 6% Sr substitution [35,36] whereas they peak at $x = 0.520$ for pure PZT [11]. Thus, the MPB shifts by $\Delta x \simeq 0.01$ on 6% Sr^{2+} substitution at the Pb^{2+} site. However, the symmetries of the phases across the MPB and in the MPB region remain exactly the same. This was shown in our earlier papers [22,32,37] for 6% Sr substitution. No new crystallographic phase emerges as a result of 6% Sr substitution. It is therefore not expected that the same materials prepared by the solid-state route will introduce new phases in the phase diagram of PSZT or PZT. The solid solution route can increase the width of the MPB region due to compositional homogeneities in the samples. This has been discussed in our early papers related to the location of MPB width for the semiwet route [38]. Figure 1 of the Supplemental Material [39] gives high-resolution SXRPD collected at room temperature to confirm that our samples are single phase and they show the features identical to those for pure PZT, other than a shift in the MPB by $\Delta x \simeq 0.01$. With these remarks about our sample *vis-à-vis* PZT, we now proceed to describe phase transitions in PSZT.

A. Antiferrodistortive phase transition in PSZT compositions with $0.65 \leqslant x \leqslant 0.90$: Dielectric studies

As mentioned earlier, the phase transitions on the Zr^{4+}-rich side of PZT are driven by both FD polar and AFD antiphase rotational instabilities occurring at T_c and T_{AFD} with $T_{AFD} < T_c$. The ferroelectric or polar transition at T_c gives rise to a huge peak in the real part of the dielectric permittivity. Figure 1 depicts the temperature dependence of the real (ε') and imaginary parts (ε'') of the dielectric permittivity for PSZT compositions with $x = 0.65, 0.70, 0.80, 0.85$, and 0.90. For comparison, we have also included the $\varepsilon'(T)$ plot for a typical tetragonal composition with $x = 0.40$. It is evident from the figure that with the increase in Zr^{4+} content, the Curie temperature (T_c) decreases. The sudden upward trend in the dielectric permittivity (ε') above T_c for some compositions is due to the increase in the conductivity of the samples at lower frequencies.

The $\varepsilon'(T)$ variation for $x \geqslant 0.65$ is not sharp but rather diffuse as compared to the relatively sharp $\varepsilon'(T)$ for the tetragonal composition with $x = 0.40$ (see Fig. 1). It is interesting to note that the diffuseness of the $\varepsilon'(T)$ initially increases with increasing x but starts decreasing for $x \geqslant 0.850$. The ferroelectrics showing such diffuse phase transitions exhibit significant deviations from the Curie-Weiss law and often exhibit relaxor ferroelectric behavior [40,41]. For relaxor ferroelectrics, the temperatures T_m' and T_m'' corresponding to the peaks in $\varepsilon'(T)$ and $\varepsilon''(T)$ plots shift to higher temperatures on

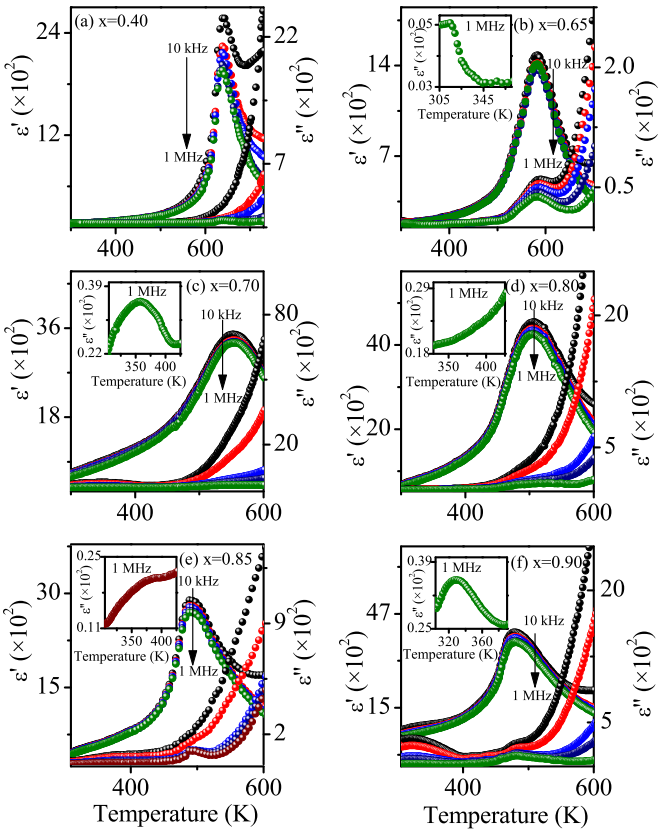

FIG. 1. (Color online) Temperature dependence of the real (ε') and imaginary (ε'') parts of the dielectric permittivity of PSZT for (a) $x = 0.40$, (b) $x = 0.65$, (c) $x = 0.70$, (d) $x = 0.80$, (e) $x = 0.85$, and (f) $x = 0.90$ at various frequencies (10, 50, 100, 500 kHz, and 1 MHz). The insets show the variation in ε'' with temperature at 1 MHz frequency in the selected temperature range.

increasing the frequencies of measurement. In addition, T_m'' is less than T_m'. However, the $\varepsilon'(T)$ data shown in Fig. 1 reveal that $T_m' = T_m'' = T_c$ and it does not shift with increasing frequency of measurement. This suggests that the diffuse phase transition in PSZT on the Zr^{4+}-rich side of the MPB is of nonrelaxor type as has been reported in other disordered ferroelectrics, such as $Pb(Fe_{0.50}Nb_{0.50})O_3$ [42].

Such diffuse transitions have generally been explained in terms of local transition temperatures in different regions of the sample with respect to the average transition temperature T_c due to statistical fluctuations in the composition [40,41,43,44]. The dielectric measurements correspond to the superimposition of contributions from individual regions with their characteristic transition temperatures giving rise to an average Curie transition temperature T_c with a Curie range of temperatures (ΔT_c) over which the transition is spread out. Assuming a Gaussian-type fluctuation in local T_c, it has been shown that the critical exponent for $\varepsilon'(T)$ would be 2 for such diffuse phase transitions [43],

$$\frac{1}{\varepsilon'} - \frac{1}{\varepsilon_m'} = \frac{[T - T_m']^2}{2\delta^2}, \tag{1}$$

where 2δ is the width of the Gaussian and determines the extent of the diffuseness of the phase transition. However, in

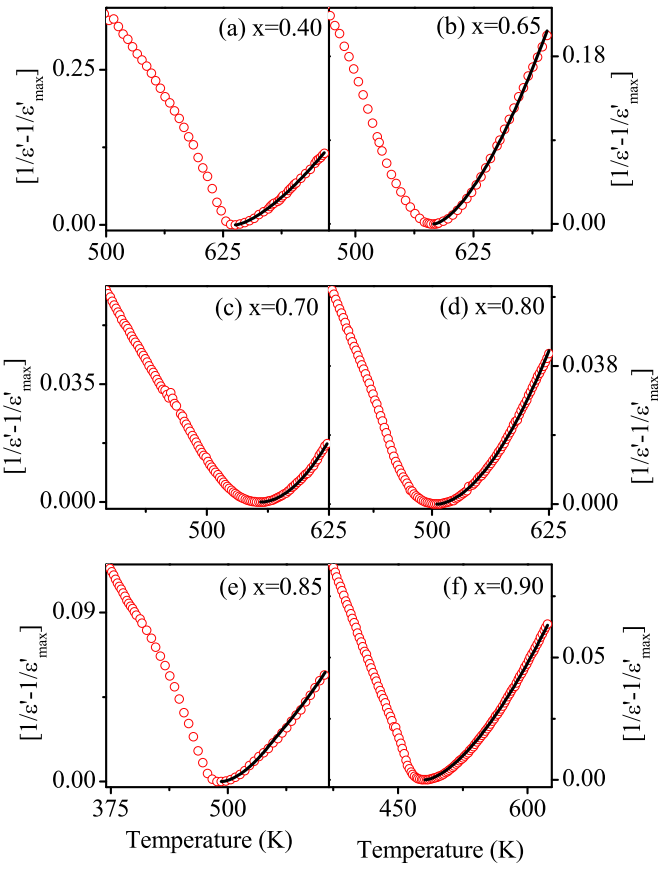

FIG. 2. (Color online) Temperature dependence of $[1/\varepsilon' - 1/\varepsilon'_m]$ for PSZT for (a) $x = 0.40$, (b) $x = 0.65$, (c) $x = 0.70$, (d) $x = 0.80$, (e) $x = 0.85$, and (f) $x = 0.90$ using dielectric data at 1 MHz. The continuous dark line is the fit to the modified Curie-Weiss law [Eq. (2) in the text] with an exponent $1 < \gamma < 2$.

several systems, the critical exponent has been reported to lie in the range of $1 < \gamma < 2$, where $\gamma = 1$ corresponds to the ideal mean-field Curie-Weiss behavior. We have determined γ as a function of composition using the following empirical relationship, which is a generalization of Eq. (1) [44]:

$$\frac{1}{\varepsilon'} - \frac{1}{\varepsilon'_m} = \frac{[T - T'_m]^\gamma}{C}. \tag{2}$$

Figure 2 shows the fits for the above relationship for PSZT with $x = 0.40$, 0.65, 0.70, 0.80, 0.85, and 0.90. The value of γ is found to be 1.47, 1.57, 1.91, 1.79, 1.69, and 1.58, respectively.

The physics of such diffuse transitions due to quenched (frozen-in) disorder has been discussed by Imry and Wortice [45] for first-order phase transitions. This theory takes into account the concept of fluctuations in local transition temperatures due to frozen-in disorder as was considered empirically in early literature on diffuse ferroelectric transitions leading to Eqs. (1) and (2) [43,44]. The essential argument behind the Imry and Wortice [45] theory is that the correlation length and the transition depend on the local composition (i.e., the distribution of the frozen-in disorder) and because of that the transition can get smeared provided the interfacial energy associated with finite-size transformed clusters with their own characteristics transition temperatures can be recovered from the chemical free-energy gain due to the local paraelectric to ferroelectric phase transition.

In PSZT, we have dilute disorder at the Pb^{2+} site due to 6% Sr^{2+} substitution and significant frozen-in disorder at the Zr^{4+} site due to the substitution by Ti^{4+}. This is frozen-in disorder or quenched disorder as it cannot be annealed out. If quenched disorder can be annealed out, Ti^{4+} and Zr^{4+} should be ordered giving rise to superstructures. The PSZT samples used by us are the annealed powders obtained from the crushing of sintered pellets. No evidence for Zr^{4+} and Ti^{4+} ordering is observed after annealing, and therefore, the disorder introduced by Ti^{4+} substitution is random and quenched in or frozen in. In such disordered systems, statistical fluctuation in local composition is the main cause for the diffuse nature of ferroelectric phase transition. Since such a smearing of $\varepsilon'(T)$ has been reported in Zr^{4+}-rich compositions of PZT also [46], we believe that the smearing of $\varepsilon'(T)$ in PSZT shown in Fig. 1 is essentially due to the substitution of Ti^{4+} at the Zr^{4+} site of $PbZrO_3$. This is why the transition becomes more diffuse on moving away from the $PbZrO_3$ end with a gradually increasing value of γ from 1.58 for $x = 0.90$ to 1.91 for $x = 0.70$. The value of γ for $x = 0.70$ is close to 2 expected for Gaussian distribution of T_c. For a further increase in Zr^{4+} content, γ again starts decreasing as for the MPB compositions near $x = 0.50$, the concept of Ti^{4+} as a substitutional disorder in the Zr^{4+} lattice loses meaning. Microscopically, the difference in the ionic radii of Zr^{4+} ($r \sim 0.72$ Å) and Ti^{4+} ($r \sim 0.605$ Å) leads to larger Zr-O bond lengths (~2.1 Å) as compared to Ti-O (~1.9-Å) bond lengths in PZT as confirmed by pair distribution function analysis [47], density functional theory calculations [48], and x-ray absorption fine-structure experiments [49]. It has been found that the off-center displacement of Zr^{4+} in an oxygen octahedral cage is less than that of the Ti^{4+} in the ferroelectric phase. This difference may be responsible for the strong disorder effect due to substitution of Ti^{4+} at the Zr^{4+} site.

The $\varepsilon'(T)$ plots do not reveal any signature of the AFD transition below T_c, except for one composition, i.e., $x = 0.90$, for which a steplike change is observed at the AFD transition. A steplike anomaly at the T_{AFD} appears because of the coupling between the polar and the AFD modes but is generally overwhelmed by the strong overlapping contribution from the polar mode [30]. Since the relative strength of the AFD mode increases whereas that of the polar mode decreases on approaching the $PbZrO_3$ end, the signature of the AFD transition in $\varepsilon'(T)$ is not observed for compositions farther away from the $PbZrO_3$ end. Interestingly, the dielectric loss [$\tan\delta$ or $\varepsilon''(T)$] gives a clearer signature of the nonpolar AFD transitions. This has been discussed in detail in the context of $SrTiO_3$ where a peak in $\varepsilon''(T)$ at cubic to tetragonal AFD phase transition is observed around $T_{AFD} \sim 105$ K without any corresponding anomaly in $\varepsilon'(T)$ (see, e.g., Ref. [50]). The peak in $\varepsilon''(T)$ at T_{AFD} has been attributed to the dynamics of domain walls which are affected by the AFD transition involving tilting of oxygen octahedra [30,51]. The peak in $\varepsilon''(T)$ shown in Fig. 1 is also due to the AFD transition as has been reported by previous workers also in the context of PZT [11,27]. However, the peak in $\varepsilon''(T)$ at the T_{AFD} peak is rather broad, and such broad peaks in dielectric loss may also occur due to extrinsic reasons, such

as defects/impurities dynamics. The defect peaks disappear at very high frequencies. In our case, as evident from the insets of Fig. 1, the peak in $\varepsilon''(T)$ is observable even at 1-MHz frequency. Furthermore, the temperature corresponding to the anomaly in $\varepsilon''(T)$ is independent of the measuring frequency, temperature rate, and thermal history and can therefore be regarded to be of intrinsic origin and linked with the AFD transition involving tilting of oxygen octahedra. The reason why we did not observe the peak in $\varepsilon''(T)$ for $x = 0.80$ was due to the overwhelming contribution of the σ_{AC} of the samples. It is evident from Fig. 1 that T_{AFD} is above room temperature for all the compositions and is found to initially increase with increasing Zr^{4+} content, reach a maximum for $x \approx 0.85$, and then start decreasing in agreement with similar observations for undoped PZT. It is worth mentioning here that recently Cordero *et al.* [30] have observed such diffuse anomalies in undoped PZT in the imaginary part of dielectric susceptibility (χ'') and elastic compliance (s'') around the T_{AFD} and they have established the temperature-composition ($T - x$) phase diagram of PZT using these data. The temperature corresponding to the peak in $\varepsilon''(T)$ for our samples of PSZT is in agreement with the disappearance of the superlattice peaks in SXRPD patterns as discussed below.

B. Structural evidence for antiferrodistortive phase transition: SXRPD studies

In this section, we consider the evolution of SXRPD profiles of PSZT as a function of temperature for a representative composition with $x = 0.65$. Figure 3 depicts the synchrotron x-ray powder diffraction profiles of the $(3/2\ 1/2\ 1/2)_{pc}$ superlattice reflection and $(200)_{pc}$, $(220)_{pc}$, and $(222)_{pc}$ perovskite reflections as a function of temperature for $(Pb_{0.94}Sr_{0.06})(Zr_{0.65}Ti_{0.35})O_3$ (PSZT65). On increasing the temperature, the intensity of the $(3/2\ 1/2\ 1/2)_{pc}$ superlattice peak decreases and vanishes above $\simeq$ 315 K in agreement with the T_{AFD} obtained by dielectric studies discussed in the previous section. Although the superlattice peak vanishes above $T_{AFD} \simeq 315$ K, the asymmetric nature of the $(222)_{pc}$ reflection still persists above T_{AFD}. On increasing the temperature further, all the profiles eventually become singlets and symmetric as expected for the cubic paraelectric phase.

For the AFD phase transitions in PZT, the tilt angle represents the primary order parameter. The intensity of the superlattice peaks is proportional to the square of the tilt angle [31]. We depict in Fig. 4(a) the temperature dependence of the integrated intensity of the $(3/2\ 1/2\ 1/2)_{pc}$ superlattice peak for PSZT65 to determine the order of the AFD phase transition. The solid line in Fig. 4(a) represents a least-squares fit for the power law $I_{(3/2\ 1/2\ 1/2)_{pc}} \sim (1 - T/T_c)^{2\beta}$, which gives an exponent of 1/2. This suggests a second-order nature of the AFD phase transition in PSZT65. The AFD phase transition in several well-known perovskites, such as $SrTiO_3$ [52] and $CaTiO_3$ [53], is also known to be second order. The second-order nature of the AFD phase transition in PSZT65 was further confirmed by the variation in unit-cell volume with the temperature depicted in Fig. 4(b). The continuous nature of volume with temperature with only a change in the slope around 315 K is consistent with the second-order nature of the AFD phase transition in PSZT65. We also observe a sharp

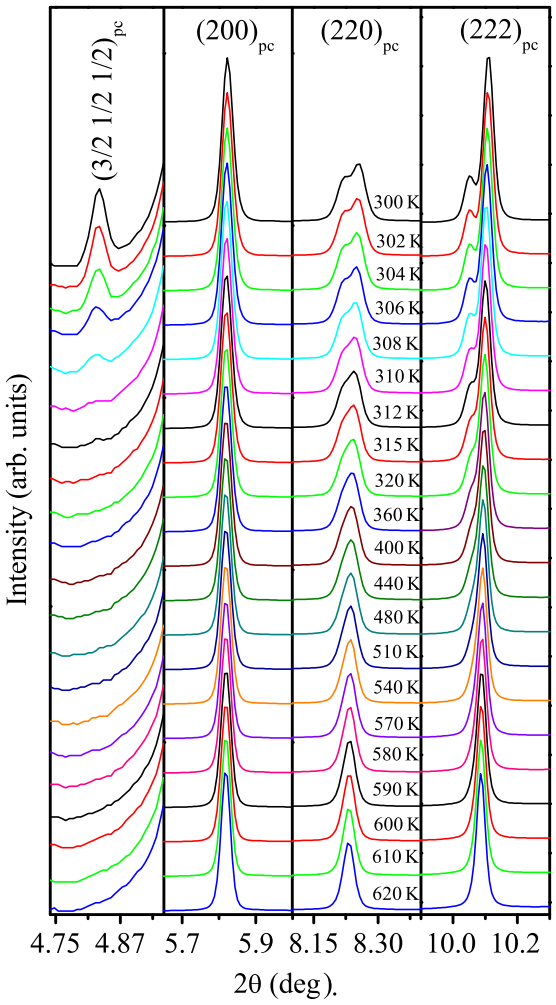

FIG. 3. (Color online) Temperature evolution of synchrotron XRPD profiles of the $(3/2\ 1/2\ 1/2)_{pc}$ superlattice reflection and $(200)_{pc}$, $(220)_{pc}$, and $(222)_{pc}$ perovskite reflections of PSZT65.

change in slope in the temperature variation of the FWHM of the $(200)_{pc}$ peak [Fig. 4(c)] around 315 K corresponding to the AFD transition at $T_{AFD} \simeq 315$ K.

As a next step, we now consider the space group symmetry of the ferroelectric phase of PSZT65 in the temperature range of $T_{AFD} < T < T_c$. In the early literature, this phase has been labeled as the F_R^{HT} phase with the $R3m$ space group, identical to the structure of PZT at room temperature for $0.530 < x < 0.620$ [11]. It is now well established [9,10] that the room-temperature structure of PZT for $0.530 < x < 0.620$ is not rhombohedral but monoclinic in the Cm space group. Accordingly, we considered both the $R3m$ and the Cm space groups as plausible models for PSZT65 at $T_{AFD} < T < T_c$. Figure 5 shows the Rietveld fits using these two space group models at $T = 360$ K. The Cm space group model gives a significantly better fit [see Figs. 5(a) and 5(b)] and lower agreement factors compared to the $R3m$ space group model. Following the results of Ref. [26], we considered the coexistence of Cm and $R3m$ phases, but this led to a zero phase fraction of the $R3m$ phase. We are thus led to conclude that the structure of PSZT65 in the temperature range of $T_{AFD} < T < T_c$ can be described using the monoclinic Cm

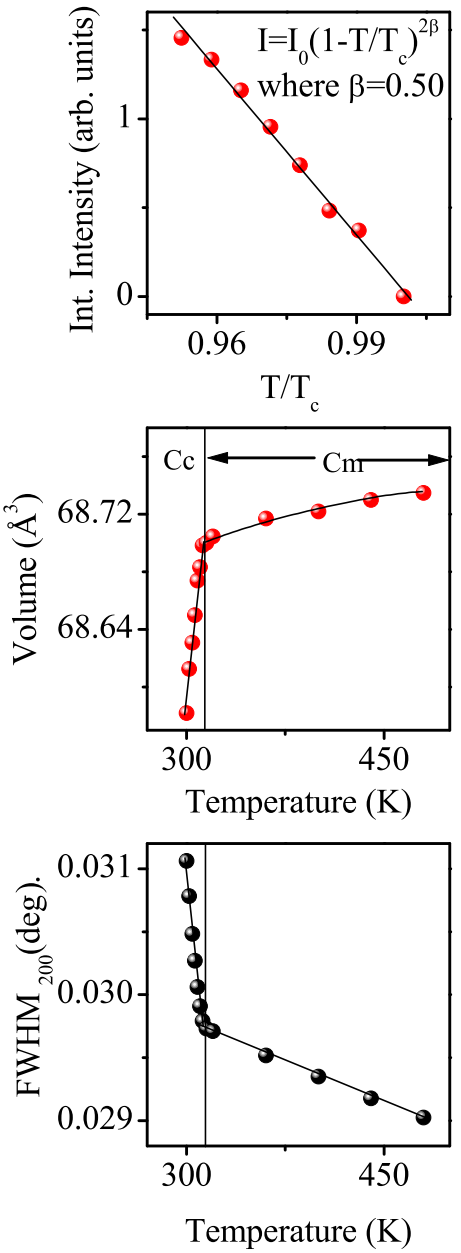

FIG. 4. (Color online) Temperature dependence of (a) integrated intensity, (b) unit-cell volume, and (c) FWHM of the $(200)_{pc}$ peak in the selected temperature region. The continuous line in (a) represents the least-squares fit using power law $I_{(3/2\ 1/2\ 1/2)_{pc}} \sim (1 - T/T_c)^{2\beta}$.

space group alone. We believe that the phase coexistence reported [26] for compositions corresponding to the Zr-rich side of the MPB with T_{AFD} above room temperature is of extrinsic origin coming from chemical inhomogeneity in the samples as discussed in the literature for PZT samples prepared by different routes [54,55].

C. Room-temperature structures of PSZT for $0.65 \leqslant x \leqslant 0.90$: SXRPD and neutron powder diffraction studies

The intensity of the superlattice peak increases as the Zr^{4+}-content increases, which implies an increase in the tilt angle [31]. This is illustrated in Fig. 1 of the Supplemental

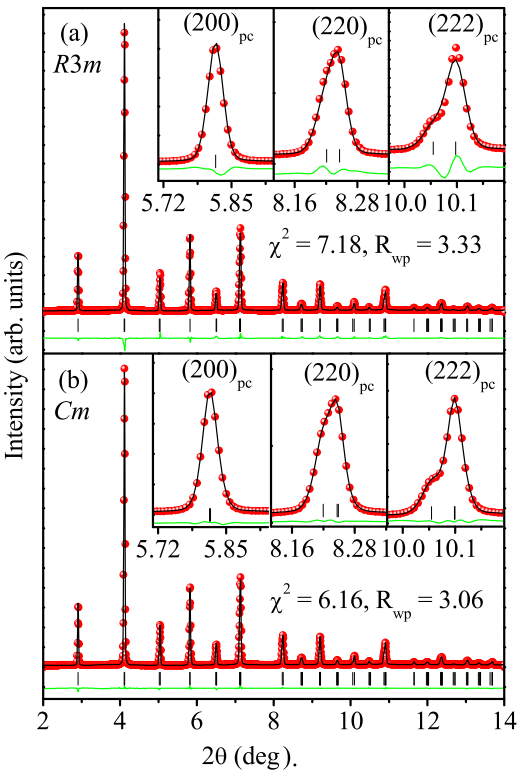

FIG. 5. (Color online) Observed (dots), calculated (continuous line), and difference (bottom line) profiles of PSZT65 at 360 K obtained after Rietveld refinement using (a) $R3m$ and (b) Cm structural models. Vertical ticks below the peaks mark the position of the Bragg reflections.

Material [39], which depicts the SXRPD patterns for $(200)_{pc}$, $(220)_{pc}$, and $(222)_{pc}$ perovskite peaks along with the most intense superlattice peak with indices $(3/2\ 1/2\ 1/2)_{pc}$ at room temperature for various compositions of PSZT in the composition range of $0.65 \leqslant x \leqslant 0.90$. The ratio of FWHM of the $(200)_{pc}$ peak to that of the nearby $(111)_{pc}$ peak for the tetragonal and rhombohedral structures should be ~1.0. However, we find that this ratio is more than 1.0 as can be seen from Fig. 2 of the Supplemental Material. This type of anisotropic broadening has been shown to be a signature of monoclinic distortion with short correlation length in the context of PZT as it cannot be modeled in terms of anisotropic strain using Stephen's model [55]. This implies that the room-temperature structure of Zr^{4+}-rich compositions of PSZT for $0.650 \leqslant x \leqslant 0.90$ may not be rhombohedral. Accordingly, we considered four different structural models for the refinement of the structure of PSZT65: (a) the $R3c$ space group without anisotropic strain broadening parameters, (b) the $R3c$ space group with anisotropic strain broadening parameters [56], (c) the Cc space group [17,25], and (d) the $R3c + Cm$ [26] space group models proposed in the literature.

Figure 6 depicts the Rietveld fits for the four structural models along with their agreement factors. We first consider the $R3c$ space group model without anisotropic strain broadening parameters. The fits are shown in Fig. 6(a). This structural model is not able to account for the additional broadening of the $(200)_{pc}$ peak. Also, the intensity of the

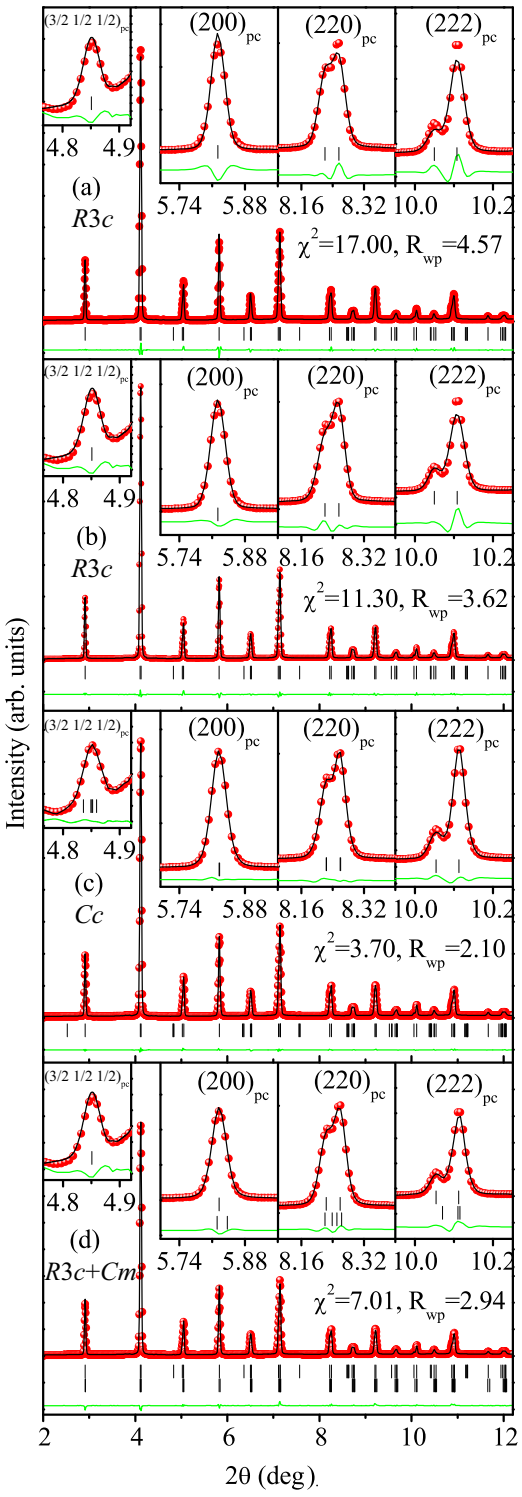

FIG. 6. (Color online) The observed (dots), calculated (continuous line), and difference (bottom) SXRPD profiles for the $(3/2\ 1/2\ 1/2)_{pc}$ superlattice and $(200)_{pc}$, $(220)_{pc}$, $(222)_{pc}$ perovskite peaks obtained after Rietveld refinement of the structure of PSZT65 at room temperature using (a) the $R3c$ space group without anisotropic strain broadening parameters, (b) the $R3c$ space group with anisotropic strain broadening parameters, (c) the Cc space group, and (d) the $R3c + Cm$ space group models.

$(200)_{pc}$, $(220)_{pc}$, and $(222)_{pc}$ peaks is not accountable with this model. Furthermore, this space group model gives very high values for χ^2 (17.00) and R_{wp} (4.57). We then considered the $R3c$ space group model with anisotropic strain broadening parameters. It is evident from the difference profile (bottom line) of Fig. 6(b) that the $R3c$ space group model with anisotropic strain broadening parameters improves the fits and reduces the χ^2 (11.30) significantly but the mismatch between the observed and calculated peak profiles still persists. The Cc space group model, proposed by Pandey *et al.* [17] and Fraysse *et al.* [25], on the other hand, gives an excellent fit between the observed and the calculated profiles of the superlattice as well as the main perovskite reflections with a drastically lower value of χ^2 (3.70) in comparison to the $R3c$ space group model [see Fig. 6(c)]. Rietveld fits corresponding to the coexistence of the $R3c$ and Cm space group models proposed recently by some workers [26] for Zr^{4+}-rich compositions of PZT are shown in Fig. 6(d). Evidently, the $R3c + Cm$ model also gives a significantly higher value of χ^2 (7.01) than the Cc space group model, even though the latter has a lesser number of refinable parameters (35) in comparison to the former (43). We can, therefore, rule out the $R3c$ and $R3c + Cm$ space group models proposed in Ref. [26] for the room-temperature superlattice phase of PZT for Zr^{4+}-rich compositions. Combining the results of the previous and the present sections, we thus conclude that the AFD transition occurs between two monoclinic phases in the Cm and Cc space groups stable above and below T_{AFD}, respectively.

On the same basis as discussed above for PSZT65, we carried out refinements of room-temperature SXRPD patterns for other Zr^{4+}-rich compositions using the Cc space group model, and they are shown in Fig. 7. The fits for all the compositions are quite good with nearly flat difference profiles. The intensity of the superlattice peaks resulting from the tilting of oxygen octahedra is rather small in Fig. 1of the Supplemental Material [39] due to relatively weak scattering of x rays from lighter atoms, such as oxygen. Neutrons, on the other hand, are scattered by the nuclei of atoms, and neutron-scattering length does not vary with atomic number in a regular manner. Because of this, light elements, such as oxygen, etc., also produce relatively strong scattering. So, to complement our SXRPD studies, we refined the structure of PSZT using neutron powder diffraction patterns also for two compositions with $x = 0.65$ (PSZT65) and $x = 0.70$ (PSZT70). We considered the same structural models as in the refinements using SXRPD data. The Rietveld fits corresponding to $R3c$ and $R3c + Cm$ space group models reveal a significant mismatch between the observed and the calculated profiles of the $(3/2\ 1/2\ 1/2)_{pc}$ superlattice peak. The calculated profile for this peak is not able to capture the width of the observed profile [Figs. 8(a) and 8(b), and 9(a) and 9(b)]. This mismatch is highlighted with arrows in the figure. The Cc space group model gives a much better fit in comparison to $R3c$ and $R3c + Cm$ models to the superlattice $(3/2\ 1/2\ 1/2)_{pc}$ peak with the lowest χ^2 values for both compositions [see Fig. 8(c)]. We can therefore rule out the $R3c$ and $R3c + Cm$ structural models for PSZT65 and 70 using Rietveld analysis of the neutron powder diffraction data also. The first rows of Figs. 8 and 9 depict the Rietveld fits around the $(1/2\ 1/2\ 1/2)_{pc}$ superlattice position, which is expected for the Cc space group model but is extinguished for the $R3c$

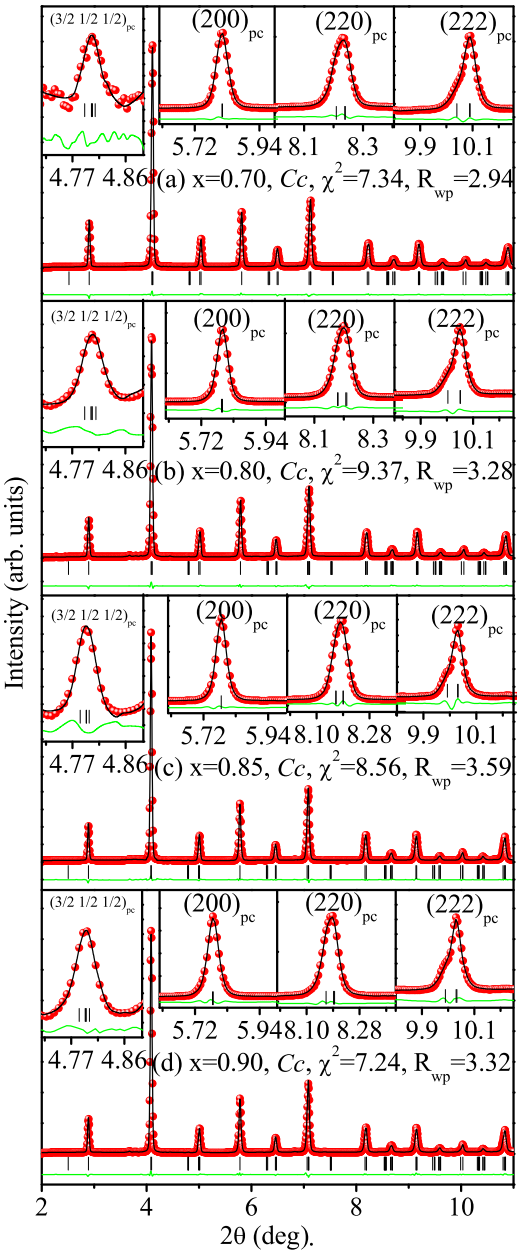

FIG. 7. (Color online) Observed (open circles), calculated (solid line), and difference (bottom line) patterns obtained from the Rietveld analysis of the room-temperature synchrotron XRPD data of PSZT70, 80, 85, and 90 using the Cc space group model. The vertical tick marks above the difference line stand for the Bragg peak positions.

and $R3c + Cm$ models [26]. The intensity of this peak is about ~0.02% of the highest intensity $(111)_{pc}$ perovskite peak of the neutron powder diffraction pattern whereas the background noise level is ~0.03%. We therefore do not expect to resolve the $(1/2\ 1/2\ 1/2)_{pc}$ peak in our neutron diffraction pattern. Based on our Rietveld refinements using SXRPD and neutron powder diffraction patterns, we thus conclude that the ground state of PSZT in the composition range of $0.620 \lesssim x \lesssim 0.940$ and below T_{AFD} corresponds to a monoclinic phase in the Cc space group confirming the proposal of Pandey *et al.* [17].

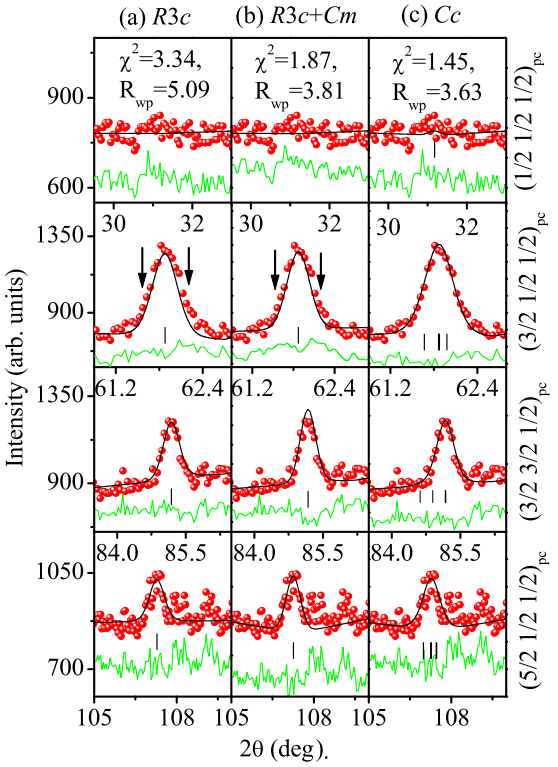

FIG. 8. (Color online) The observed (dots), calculated (continuous line), and difference (bottom) neutron diffraction profiles for PSZT65 for the $(3/2\ 1/2\ 1/2)_{pc}$, $(3/2\ 3/2\ 1/2)_{pc}$, and $(5/2\ 1/2\ 1/2)_{pc}$ superlattice peaks obtained after Rietveld refinement of the structure at room temperature using the (a) $R3c$, (b) $R3c + Cm$, and (c) Cc space group models. The first row of the figure shows the zoomed view around the $(1/2\ 1/2\ 1/2)_{pc}$ superlattice reflection.

D. Phase diagram of PSZT for $0.40 \leqslant x \leqslant 0.90$

On the basis of the high-resolution SXRPD, neutron powder diffraction, dielectric, and sound velocity studies carried out in our previous and in the present papers, we have constructed a temperature-composition (T-x) phase diagram of PSZT for $0.40 \leqslant x \leqslant 0.90$ shown in Fig. 10. Compositions in the range of $0.51 \leqslant x \leqslant 0.550$ were prepared by the semiwet route. A full description of the sample preparation has been given in our previous paper [22]. The paraelectric to ferroelectric phase boundary (red dots) for compositions with $0.51 \leqslant x \leqslant 0.550$ were determined from the temperature-dependent dielectric studies during heating cycles [32]. Dielectric studies for these compositions show the vanishing of thermal hysteresis for $x \simeq 0.550$ [32] due to a crossover from first-order to second-order phase transition at a tricritical point at $x \simeq 0.550$. Using Rietveld analysis of temperature-dependent SXRPD studies, it was shown that compositions with $0.515 \leqslant x \leqslant 0.545$ undergo cubic to tetragonal phase transition and then transform to the pseudotetragonal monoclinic phase whereas the compositions with $0.550 \lesssim x \lesssim 0.940$ directly transform to the pseudorhombohedral monoclinic phase. This leads to a triple point in the phase diagram at $x \simeq 0.550$ coinciding with or very close to a tricritical point [32]. We show in Fig. 10 the magnified view of this region to highlight the various phases in and around the tricritical point. The low-temperature

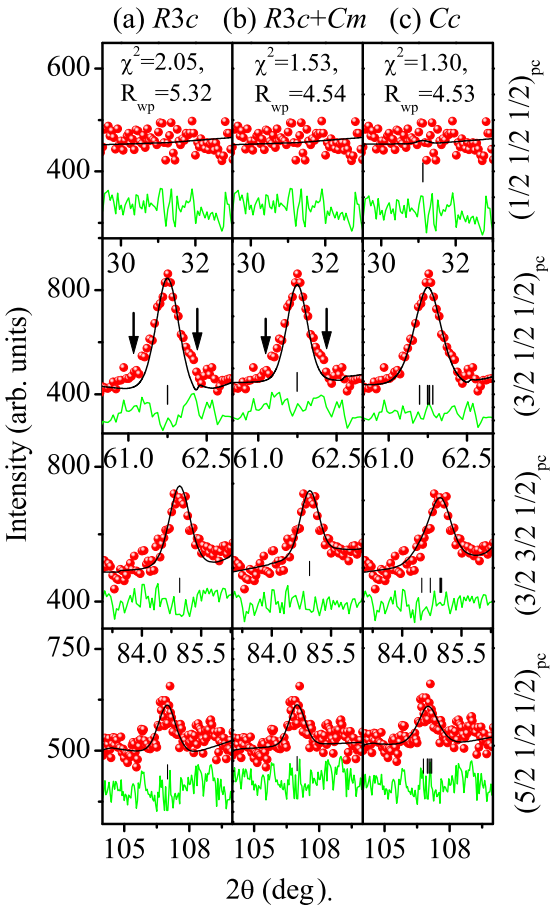

FIG. 9. (Color online) The observed (dots), calculated (continuous line), and difference (bottom) neutron diffraction profiles for PSZT70 for the $(3/2\ 1/2\ 1/2)_{pc}$, $(3/2\ 3/2\ 1/2)_{pc}$, and $(5/2\ 1/2\ 1/2)_{pc}$ superlattice peaks obtained after Rietveld refinement of the structure at room temperature using the (a) $R3c$, (b) $R3c + Cm$, and (c) Cc space group models. The first row of the figure shows the zoomed view around the $(1/2\ 1/2\ 1/2)_{pc}$ superlattice reflection.

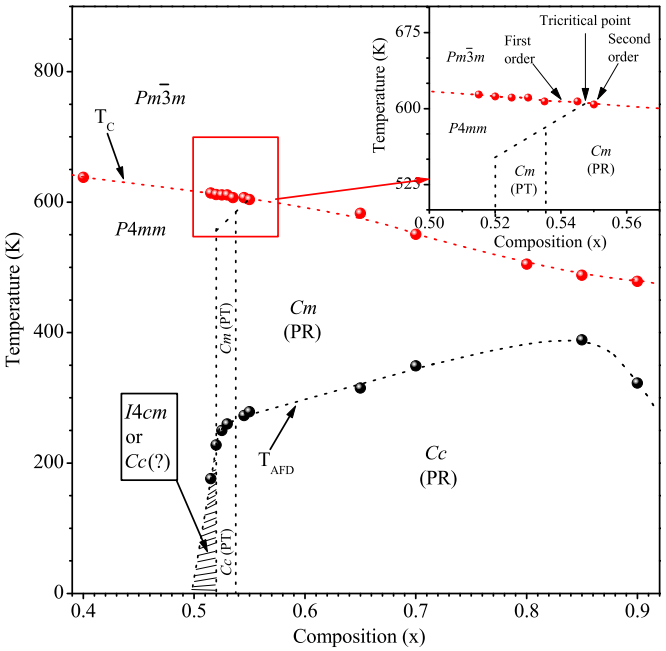

FIG. 10. (Color online) Schematic phase diagram of PSZT constructed on the basis of neutron, synchrotron, sound velocity, and dielectric measurements. The red dots in the phase diagram correspond to the high-temperature cubic ($Pm\bar{3}m$) to tetragonal ($P4mm$) and cubic to the pseudorhombohedral monoclinic (Cm) phase-transition temperatures during heating, obtained from dielectric measurements. The black dots correspond to the low-temperature antiferrodistortive (T_{AFD}) phase (space group Cc) transition temperatures. For $0.515 \leqslant x \leqslant 0.550$, T_{AFD} was determined from the sound velocity measurements [32] whereas for $0.65 \leqslant x \leqslant 0.90$, it was determined from the temperature dependence of ε''. The symbols PT and PR represent pseudotetragonal and pseudorhombohedral monoclinic phases, respectively. The vertical lines are first-order phase boundaries across which the two neighboring phases coexist. Also, the inclined $P4mm - Cm$ (PT)/Cm (PR) phase boundary is a first-order phase boundary. T_c stands for the Curie temperature, and T_{AFD} stands for the antiferrodistortive phase-transition temperature. The inset shows the magnified view of the figure around the tricritical point established in Ref. [32].

ferroelectric to antiferrodistortive phase boundary (black dots) for the compositions with $0.515 \leqslant x \leqslant 0.550$ was established using temperature-dependent sound velocity measurements. The symmetries below the T_{AFD} were confirmed to be monoclinic in the Cc space group [22,37] except for $x = 0.515$. The space group of the low-temperature phase of PSZT515 may be $I4cm$ or Cc [17,23], but more work is needed to settle this issue, as there is no intermediate monoclinic Cm phase between the tetragonal and the lowest temperature phase. The vertical dotted lines in Fig. 10 are the first-order lines which separate the tetragonal and pseudorhombohedral monoclinic phases. MPB in PSZT lies in the range $0.520 \lesssim x \lesssim 0.535$ [22]. For $0.520 \lesssim x \lesssim 0.525$, the pseudotetragonal monoclinic phase in the Cm space group and the tetragonal phase in the $P4mm$ space group are the stable phases whereas for $0.525 \leqslant x \lesssim 0.535$ pseudotetragonal and pseudorhombohedral monoclinic phases both in the Cm space group coexist. According to Mishra [35] and Lal *et al.* [36], the maximum in physical properties, such as electromechanical coupling coefficient, piezoelectric strain coefficient, and dielectric constant, occurs for $x = 0.530$. Thus MPB in PSZT is shifted by ∼1% to the Zr-rich side in comparison to undoped PZT where the maximum in physical properties occurs at $x \simeq 0.520$. Ti-rich compositions of PZT undergo only a high-temperature paraelectric cubic to ferroelectric tetragonal phase transition. We have determined the Curie temperature (T_c) in this composition range using dielectric measurements.

The phase boundary for the composition range of $0.65 \leqslant x \leqslant 0.90$ with T_{AFD} lying above room temperature (300 K) has been determined using the anomalies in dielectric loss shown in Fig. 1. It is evident that T_{AFD} determined using sound velocity measurements below room temperature for $x < 0.620$ and those determined using dielectric measurements above room temperature for $0.620 < x < 0.940$ follow the same trend as in the case of pure PZT [11,17]. It increases on increasing the Zr content up to $x \gtrsim 0.850$ nearly linearly and then decreases. Ferroelectric T_c for Zr-rich compositions with $0.650 \leqslant x \leqslant 0.90$ have been determined from the real (ε') part of the dielectric constant discussed in Sec. III A and

shown in Fig. 1. The symmetries of the various phases above and below T_{AFD} as discussed in Secs. III B and III C have been determined using SXRPD and neutron powder diffraction studies. For $T < T_{AFD}$ symmetry of Zr-rich compositions is monoclinic in the Cc space group whereas for $T_{AFD} < T < T_c$, the symmetry is also monoclinic but in the Cm space group. All the compositions transform to the cubic paraelectric phase in the $Pm\bar{3}m$ space group above their corresponding Curie temperature (T_c), and T_c decreases with increasing $PbZrO_3$ content as expected from the lower T_c of $PbZrO_3$. Here, it is important to emphasize that 6% Sr^{2+} substitution does not alter the phase stabilities of PZT significantly, and the PSZT phase diagram is topologically similar to that of pure PZT.

IV. CONCLUSIONS

This study has led to several important findings regarding the nature of AFD phase transition on the Zr^{4+}-rich side of PZT and its phase diagram. First, we have resolved the existing controversies about the structures of PZT above and below the T_{AFD} for the composition range of $0.620 \lesssim x \lesssim 0.940$ using 6% Sr^{2+}-substituted samples. Only the Cc space group model with a lesser number of refinable parameters in comparison to the $R3c$ [11] or $R3c + Cm$ [26] structural models gives lower values of χ^2 and R_{wp} and can account for the width of the $(3/2\ 1/2\ 1/2)_{pc}$ superlattice peak in the neutron powder diffraction patterns. Our results thus rule out the $R3c$ and $R3c + Cm$ structural models proposed in recent years [26] and confirm that the Cc space group model represents the true structure of the ground-state phase of PZT at $T < T_{AFD}$ for the composition range of $0.620 \lesssim x \lesssim 0.940$. Also, the temperature dependence of the volume and integrated intensity for PSZT65 shows that AFD phase transition is of second-order type. Second, we have also shown that the high-temperature ferroelectric phase at $T_{AFD} < T < T_c$ has got the Cm space group and not the $R3m$ or $R3m + Cm$ as proposed in several recent studies [26]. Third, the phase diagram of PSZT for the composition range of $0.40 \leqslant x \leqslant 0.90$ has been established using neutron powder diffraction, synchrotron x-ray powder diffraction, dielectric, and sound velocity studies of the present and previous papers [22,32,37]. In contrast to the old phase diagram of PZT given in the standard texts [11], it is shown that all the compositions of PSZT with $0.515 \lesssim x \lesssim 0.90$ exhibit the AFD phase transition involving two monoclinic phases in the Cm and Cc space groups stable above and below T_{AFD}, respectively. The T_{AFD} of the compositions in the range of $0.515 \lesssim x \lesssim 0.62$ lies below room temperature whereas for $0.62 < x \lesssim 0.90$, it lies above the room temperature. Because of the tilted nature of MPB, a $P4mm$ to Cm polymorphic phase transition precedes the Cm to Cc AFD phase transition for the composition range of $0.515 < x \lesssim 0.550$. The present paper along with our previous findings [9,10,17] show that the monoclinic Cm phase and not the $R3m$ phase is stable above the T_{AFD} line in the entire $T - x$ plane on the Zr^{4+}-rich side of the MPB. Our results thus confirm the phase diagram proposed by Pandey *et al.* [17] for undoped PZT and reject the alternative structural models below and above T_{AFD} [26,28,56] and alternative phase diagrams proposed in some recent studies [11,23,26].

ACKNOWLEDGMENTS

D. Pandey acknowledges financial support from the Science and Engineering Research Board (SERB), Department of Science and Technology (DST), Govt. of India through the award of a J. C. Bose National Fellowship grant. R. S. Solanki acknowledges financial support from SERB, India in the form of a research assistantship under the same J. C. Bose National Fellowship. We acknowledge the assistance of Dr. M. Hinterstein from PETRA III, Deutsches Elektronen-Synchrotron (DESY), Germany in the collection of the SXRPD data. Authors R.S.S. and D.P. acknowledge financial support from the Saha Institute of Nuclear Physics (SINP), Kolkata, India under the Department of Science and Technology (DST), Govt. of India, funded "India-DESY Germany" project to carry out SXRPD experiments at DESY, Germany.

[1] R. Blinc and B. Zeks, *Soft Modes in Ferroelectrics and Antiferroelectrics* (North Holland, Oxford, 1974), p. 1.
[2] A. D. Bruce and R. A. Cowley, Adv. Phys. **29**, 219 (1980).
[3] M. E. Lines and A. M. Glass, *Principles and Applications of Ferroelectrics and Related Materials* (Clarendon, Oxford, 1977), p. 241.
[4] H. Unoki and T. Sakudo, J. Phys. Soc. Jpn. **23**, 546 (1967).
[5] P. A. Fleury, J. F. Scott, and J. M. Worlock, Phys. Rev. Lett. **21**, 16 (1968).
[6] R. A. Cowley, W. J. L. Buyers, and G. Dolling, Solid State Commun. **7**, 181 (1969).
[7] S. K. Mishra and D. Pandey, Appl. Phys. Lett. **95**, 232910 (2009).
[8] J. P. Patel, A. Singh, and D. Pandey, J. Appl. Phys. **107**, 104115 (2010); A. Singh, A. Senyshyn, H. Fuess, and D. Pandey, *ibid.* **110**, 024111 (2011).
[9] Ragini, R. Ranjan, S. K. Mishra, and D. Pandey, J. Appl. Phys. **92**, 3266 (2002).
[10] A. K. Singh, D. Pandey, S. Yoon, S. Baik, and N. Shin, Appl. Phys. Lett. **91**, 192904 (2007).
[11] B. Jaffe, W. R. Cook, and H. Jaffe, *Piezoelectric Ceramics* (Academic, London, 1971), p. 135.
[12] S. K. Mishra, D. Pandey, and A. P. Singh, Appl. Phys. Lett. **69**, 1707 (1996).
[13] S. K. Mishra, A. P. Singh, and D. Pandey, Philos. Mag. **76**, 213 (1997).
[14] B. Noheda, D. E. Cox, G. Shirane, J. A. Gonzalo, L. E. Cross, and S. E. Park, Appl. Phys. Lett. **74**, 2059 (1999); B. Noheda, J. A. Gonzalo, L. E. Cross, R. Guo, S.-E. Park, D. E. Cox, and G. Shirane, Phys. Rev. B **61**, 8687 (2000).
[15] Ragini, S. K. Mishra, D. Pandey, H. Lemmens, and G. V. Tendeloo, Phys. Rev. B **64**, 054101 (2001).
[16] R. Ranjan, Ragini, S. K. Mishra, D. Pandey, and B. J. Kennedy, Phys. Rev. B **65**, 060102(R) (2002).
[17] D. Pandey, A. K. Singh, and S. Baik, Acta Crystallogr., Sect. A: Found. Crystallogr. A **64**, 192 (2008).

[18] D. M. Hatch, H. T. Stokes, R. Ranjan, Ragini, S. K. Mishra, D. Pandey, and B. J. Kennedy, Phys. Rev. B **65**, 212101 (2002).
[19] D. E. Cox, B. Noheda, and G. Shirane, Phys. Rev. B **71**, 134110 (2005).
[20] D. I. Woodward, J. Knudsen, and I. M. Reaney, Phys. Rev. B **72**, 104110 (2005).
[21] J. Rouquette, J. Haines, V. Bornand, M. Pintard, P. Papet, W. G. Marshall, and S. Hull, Phys. Rev. B **71**, 024112 (2005).
[22] R. S. Solanki, A. K. Singh, S. K. Mishra, S. J. Kennedy, T. Suzuki, Y. Kuroiwa, C. Moriyoshi, and D. Pandey, Phys. Rev. B **84**, 144116 (2011).
[23] I. A. Kornev, L. Bellaiche, P. E. Janolin, B. Dkhil, and E. Suard, Phys. Rev. Lett. **97**, 157601 (2006).
[24] R. S. Solanki, S. K. Mishra, A. Senyshyn, S. Yoon, S. Baik, N. Shin, and D. Pandey, Appl. Phys. Lett. **102**, 052903 (2013).
[25] G. Fraysse, J. Haines, V. Bornand, J. Rouquette, M. Pintard, P. Papet, and S. Hull, Phys. Rev. B **77**, 064109 (2008).
[26] H. Yokota, N. Zhang, A. E. Taylor, P. A. Thomas, and A. M. Glazer, Phys. Rev. B **80**, 104109 (2009); D. Phelan, X. Long, Y. Xie, Z.-G. Ye, A. M. Glazer, H. Yokota, P. A. Thomas, and P. M. Gehring, Phys. Rev. Lett. **105**, 207601 (2010); N. Zhang, H. Yokota, A. M. Glazer, and P. A. Thomas, Acta Crystallogr., Sect. B: Struct. Sci. B **67**, 386 (2011).
[27] H. M. Barnett, J. Appl. Phys. **33**, 1606 (1962); D. Berlincourt, H. H. A. Krueger, and B. Jaffe, J. Phys. Chem. Solids **25**, 659 (1964).
[28] C. Michel, J. M. Moreau, G. D. Achenbach, R. Gerson, and W. J. James, Solid State Commun. **7**, 865 (1969).
[29] J. B. Goodenough, Rep. Prog. Phys. **67**, 1915 (2004).
[30] F. Cordero, F. Craciun, and C. Galassi, Phys. Rev. Lett. **98**, 255701 (2007); F. Cordero, F. Trequattrini, F. Craciun, and C. Galassi, Phys. Rev. B **87**, 094108 (2013).
[31] A. M. Glazer, Acta Crystallogr., Sect. B: Struct. Crystallogr. Cryst. Chem. B **28**, 3384 (1972); Acta Crystallogr., Sect. A: Cryst. Phys., Diffr., Theor. Gen. Crystallogr. A **31**, 756 (1975).
[32] R. S. Solanki, S. K. Mishra, C. Moriyoshi, Y. Kuroiwa, and D. Pandey, Phys. Rev. B **88**, 184109 (2013).
[33] M. Hoelzel, A. Senyshyn, N. Juenke, H. Boysen, W. Schmahl, and H. Fuess, Nucl. Instrum. Methods Phys. Res., Sect. A **667**, 32 (2012).
[34] J. Rodriguez-Carvajal, Laboratory, FULLPROF, a Rietveld and pattern matching and analysis program, version (Laboratoire Leon Brillouin, CEA-CNRS, France, 2011); Physica B **192**, 55 (1993).
[35] S. K. Mishra, Ph.D. thesis, Institute of Technology, Banaras Hindu University, 1998.
[36] R. Lal, R. Krishnan, and P. Ramakrishnan, Trans. Brit. Ceram. Soc. **87**, 99 (1988).
[37] R. S. Solanki, S. K. Mishra, A. Senyshyn, I. Ishii, C. Moriyoshi, T. Suzuki, Y. Kuroiwa, and D. Pandey, Phys. Rev. B **86**, 174117 (2012).
[38] A. P. Singh, S. K. Mishra, D. Pandey, C. D. Prasad, and R. Lal, J. Mater. Sci. **28**, 5050 (1993).
[39] See Supplemental Material at http://link.aps.org/supplemental/10.1103/PhysRevB.90.214110.
[40] G. A. Smolenskii, J. Phys. Soc. Jpn. **28**, 26 (1970).
[41] L. E. Cross, Ferroelectrics **76**, 241 (1987); **151**, 305 (1994).
[42] S. P. Singh, A. K. Singh, D. Pandey, H. Sharma, and O. Parkash, J. Mater. Res. **18**, 2677 (2003).
[43] V. V. Kirillov and V. A. Isupov, Ferroelectrics **5**, 3 (1973).
[44] K. Uchino and S. Nomura, Ferroelectrics **44**, 55 (1982).
[45] Y. Imry and M. Wortis, Phys. Rev. B **19**, 3580 (1979).
[46] I. Franke *et al.*, J. Phys. D: Appl. Phys. **38**, 749 (2005).
[47] W. Dmowski, T. Egami, L. Farber, and P. K. Davies, in *Fundamental Physics of Ferroelectrics*, edited by H. Krakauer, AIP Conf. Proc. No. 582 (AIP, New York, 2001), p. 33.
[48] I. Grinberg, V. R. Cooper, and A. M. Rappe, Nature (London) **419**, 909 (2002).
[49] D. Cao, I.-K. Jeong, R. H. Heffner, T. Darling, J.-K. Lee, F. Bridges, J.-S. Park, and K.-S. Hong, Phys. Rev. B **70**, 224102 (2004).
[50] R. Viana, P. Lunkenheimer, J. Hemberger, R. Böhmer, and A. Loidl, Phys. Rev. B **50**, 601(R) (1994).
[51] K. Fossheim and B. Berre, Phys. Rev. B **5**, 3292 (1972).
[52] M. A. Geday and A. M. Glazer, J. Phys.: Condens. Matter **16**, 3303 (2004).
[53] S. A. T. Redfern, J. Phys.: Condens. Matter **8**, 8267 (1996).
[54] P. Arigur and L. Benguigui, J. Phys. D: Appl. Phys. **8**, 1856 (1975); K. Kakegawa, J. Mohri, K. Takahashi, H. Yamamua, and S. Shirashki, Solid State Commun. **24**, 769 (1977); A. P. Wilkinson, J. Xu, S. Pattanaik, and S. J. L. Billinge, Chem. Mater. **10**, 3611 (1998).
[55] P. W. Stephens, J. Appl. Crystallogr. **32**, 281 (1999).
[56] A. M. Glazer and S. A. Mabud, Acta. Crystallogr., Sect. B: Struct. Crystallogr. Cryst. Chem. **34**, 1060 (1978).